Nanoparticle Imprint Lithography: From Nanoscale Metrology to Printable Metallic Grids

Anna Capitaine, Mehrnaz Bochet-Modaresialam, Peeranuch Poungsripong, Clémence Badie, Vasile Heresanu, Olivier Margeat, Lionel Santinacci, David Grosso, Erik Garnett, Beniamino Sciacca

Nanoparticle imprint lithography: from nanoscale metrology to printable metallic grids

Anna Capitaine,[†] Mehrnaz Bochet-Modaresialam,[‡] Peeranuch Poungsripong,[†] Clémence Badie,[†] Vasile Heresanu,[†] Olivier Margeat,[†] Lionel Santinacci,[†] David Grosso,[†] Erik Garnett,[¶] and Beniamino Sciacca[*,†]

†*Aix Marseille Univ, CNRS, CINaM, AMUtech, Marseille, 13288, France*

‡*Solnil, Marseille, 13002, France*

¶*AMOLF, Amsterdam, 1098 XG, The Netherlands*

E-mail: beniamino.sciacca@cnrs.fr

Abstract

Large scale and low-cost nanopatterning of materials is of tremendous interest for optoelectronic devices. Nanoimprint lithography has emerged in recent years as a nanofabrication strategy that is high-throughput and has a resolution comparable to that of electron-beam lithography (EBL). It is enabled by pattern replication of an EBL master into polydimethylsiloxane (PDMS), that is then used to pattern a resist for further processing, or a sol-gel that could be calcinated into a solid material. Although the sol-gel chemistry offers a wide spectrum of material compositions, metals are still difficult to achieve. This gap could be bridged by using colloidal nanoparticles as resist, but deep understanding of the key parameters is still lacking. Here, we use supported metallic nanocubes as a model resist to gain

fundamental insights of nanoparticle imprinting. We uncover the major role played by the surfactant layer trapped between nanocubes and substrate, and measure its thickness with sub-nanometer resolution by using gap plasmon spectroscopy as a metrology platform. This enables us to quantify the van der Waals (VDW) interactions responsible for the friction opposing the nanocube motion, and we find that these are almost in quantitative agreement with the Stokes drag acting on the nanocubes during nanoimprint, that is estimated with a simplified fluid mechanics model. These results reveal that a minimum thickness of surfactant is required, acting as a spacer layer mitigating van der Waals forces between nanocubes and the substrate. In the light of these findings we propose a general method for resist preparation to achieve optimal nanoparticle mobility, and show the assembly of printable Ag and Au nanocube grids, that could enable the fabrication of low-cost transparent electrodes of high material quality upon nanocube epitaxy.

Keywords

Nanoimprint; Nanocube sliding; Gap-plasmon metrology; Nanogrids; Printable nanopattern; PVP lubrication

Introduction

Controlling material geometry at the nanoscale is key to improve optoelectronic device performance, as nanostructures offer endless possibilities to control light-matter interactions through scattering, absorption and emission.[1,2] Such properties can be tuned by varying nanostructure type, size, shape and their organization on a substrate, and it is typically achieved by patterning thin films via lithography techniques followed by evaporation and lift-off or etching steps.[3,4] This energy-intensive and time-consuming process hinders the integration in commercial electronic and optical devices of nanopatterned materials that could act as metasurfaces for highly efficient polarization control, anti-reflective coatings, scatterers or transparent electrodes.[5–7] As a bottom-up alternative, nanopatterns can be fabricated from colloidal building blocks via capillary assembly in nanostructured templates.[8,9] Further thermal or chemical processing to weld adjacent nanoparticles can yield a continuous polycrystalline[10] or monocrystalline material if nanocubes are used as building blocks.[11,12] However, capillary assembly techniques are less suited for dense, continuous nanopatterns with low aspect ratio (1 nanoparticle thick), and integration in industrial processing remains challenging. Other methods such as selective laser sintering are available to fabricate metal nanopatterns, but the typical resolution is larger than conventional nanofabrication techniques.[13]

Nanoimprint lithography (NIL) emerged in recent years as a highly promising solution to build nanostructures at low cost. NIL has been widely employed to nanostructure thermoplastics as well as UV-curable and sol-gel resists over a large area. The technique consists in pattern replication from a polydimethylsiloxane (PDMS) mold (itself replicated from an electron beam lithography master) to a resist material. It thus enables the excellent spatial resolution (< 10 nm) of electron beam lithography at low cost, by ensuring intimate con-

tact between the PDMS mold and the material to be patterned.[14–17] Upon polymer curing or material hardening, the stamp is removed, leaving behind a nanostructured material,[18] that can also be used as scaffold for metal deposition[19]. Despite combining the precision of top-down techniques with the scalability offered by bottom-up approaches, NIL remains so far limited to few material classes. For example, metals, highly interesting for plasmonics,[20–23] are not straightforward to obtain because metallic precursors require the presence of organic additives, that have to be removed by subsequent heat treatments. Imprinting of nanoparticles into complex geometries has been proposed either via dispersion in commercial resists [24–28], or deposited on substrates as thin films,[29–32] followed by a sintering step at high temperature. However, the resulting materials typically exhibit high porosity, rough surfaces, shrinkage and cracking,[16,33,34] whereas material quality is of paramount importance for the fabrication of high efficiency optoelectronic and nanophotonic devices.[35–38] This is in stark contrast with the initial material quality of the building blocks, that can often be synthesized in solution by colloidal synthesis as single crystals at low temperature.[39]

To mitigate these issues, effective methods have to be developed to process a highly compact nanoparticle assembly into a continuous solid material. Minimal shrinking after calcination has been achieved in metal oxide nanopatterns by tuning the nanoparticle ink surface energy and minimizing residual organics, yielding materials with a porosity comparable to that of sol-gel processes.[40] We argue that minimization of void volume can be achieved by accurate selection of the nanoparticle geometry and by precise control of the nanoimprint dynamics. Cubic nanoparticles appear to have the ideal geometry because they enable for close-packed 2D assembly, and adjacent units have identical crystallographic orientation when assembled face to face, as a result of the 4-fold rotational invariance. This enabled to achieve monocrystalline nanopatterns upon nanocube epitaxy at near ambient temperature.[11,12] In addition, a variety of materials can be synthesized as nanocubes in solution.[41–49]

Agrawal *et al.* showed that colloidal 75 nm silver nanocubes capped with polyvinylpyrroli-

done (PVP) could be used as a resist and assembled in a close packed configuration with single particle accuracy via a home-made imprint equipment.[16] Nanocubes were deposited on a substrate from a colloidal solution containing excess PVP, ensuring they remained loosely (non-permanently) bound to the substrate after solvent evaporation (phase 1). Addition of few μL of solvent just before imprint enabled nanocubes motion over significant distances (several μm), without redispersion, and high yield assembly into PDMS trenches (phase 2). After drying, the low surface energy PDMS mold is retracted, leaving assembled nanoparticles on the substrate due to the stronger interaction. In contrast to traditional lithography-based approaches, this technique has the potential to achieve nanopatterns without the need for etching and/or lift-off, and is expected to have better crystalline quality. Additionally, compared to other nanoparticle-based imprint lithography, in which small nanoparticles (<10 nm) are dispersed in a liquid ink matrix (that is imprinted, dried and annealed), here a single layer of nanocubes is deposited on the substrate before imprinting. This approach allows to minimise the amount of polymer used, therefore simplifying its removal, but can also allow to obtain dense, continuous, low aspect ratio nanopatterns (1 nanocube thick), with a lateral resolution comparable to that of e-beam lithography, thus constituting the ideal starting block for nanocube epitaxy. A quantitative framework of the physico-chemical mechanism that enables assembly with such high fidelity is however still missing. A deeper understanding of nanoparticle imprint dynamics can boost its implementation to different substrates, different nanoparticles (type, size, geometry) and different NIL equipment, making this technique even more compelling.

First, building on the previous work,[16] we implement the technique on a commercial NIL setup. This ensures conformal contact between PDMS and substrate, allows for homogeneous and reproducible assembly at large scale, and offers an ideal platform for a thorough study of the mechanism from a quantitative perspective. Next, we investigate the nanoparticle imprint lithography mechanism by using 40 nm nanocubes as a model system. In addition to the aforementioned features, we show that the nanocube themselves, supported on a metal

substrate, can be used as highly sensitive spectroscopic probes to gain precious insights on the assembly mechanism and identifying the critical parameters. This is achieved by probing gap-plasmon cavity resonances, which enables us to reveal the importance of PVP in the assembly mechanism as a capping ligand, spacer layer (mitigating van der Waals (VDW) forces at play between the substrate and the nanocubes) and lubricant. We show that the lateral mobility of 40 nm Ag nanocubes can be quantitatively correlated with the amount of PVP trapped between nanocubes and substrate in phase 1. Comparing experimental results to simulations, it was possible to estimate the thickness of the PVP layer with a precision hardly achievable by other available techniques. This enabled to assess the magnitude of VDW interactions that oppose motion via friction, and we found an almost quantitative agreement with the Stokes drag exerted on the nanocubes by the escaping solvent in phase 2. Such quantitative framework enabled to propose optimal experimental conditions that could be promptly transferred to other colloidal materials such as 40 nm Au nanocubes.

Next, we apply these findings to obtain mm^2 nanopatterned grids reproducibly, showing the technique robustness. We emphasize that this is the starting block for the low cost fabrication of high performance metallic transparent electrodes.[5,50] Finally, we show that Au and Ag nanocube grids can be transferred to other substrates, for possible integration in flexible devices or in tandem solar cells, sometimes incompatible with classic nanopatterning strategies.

Results and discussion

Nanocube assembly on a commercial NIL setup

Assembly of 30 to 40 nm gold and silver nanocubes into grids is investigated on a commercial NIL setup using pressurized air to inflate a nanopatterned PDMS membrane and achieve a convex bottom surface and conformal contact as the mold is pressed against the substrate (Figure 1). This is expected to minimize or eliminate misalignment between the substrate and the mold, and to improve repeatability compared to previous experiments made with a homemade setup in which the mold is mounted on a rigid flat surface pressed against the substrate.[16]

The PDMS mold was patterned with 4 grids with dimension 2x2, 1x1 and 0.5x0.5 mm^2, with pitches of 4 μm, a width of 200 nm (5 nanocubes) and trenches depth of 40 nm (1 nanocube) (Figures 1 and S1). In phase 1, nanocubes were added to the substrate using convective deposition in 1 mM Sodium Dodecyl Sulfate (SDS), which enabled to control nanocube density and yielded to quasi-homogeneous substrates (phase 1, Figure 1).

Next, a droplet of solvent was deposited on the PDMS mold before pressing it against the substrate at steady speed. The magnitude of the normal force applied to the substrate was controlled by setting inflating pressure and PDMS mold final position (phase 2, Figure 1). The substrate was then heated to 55°C for 30 minutes, while maintaining PDMS position and pressure, to ensure for complete solvent drying before retracting the stamp.

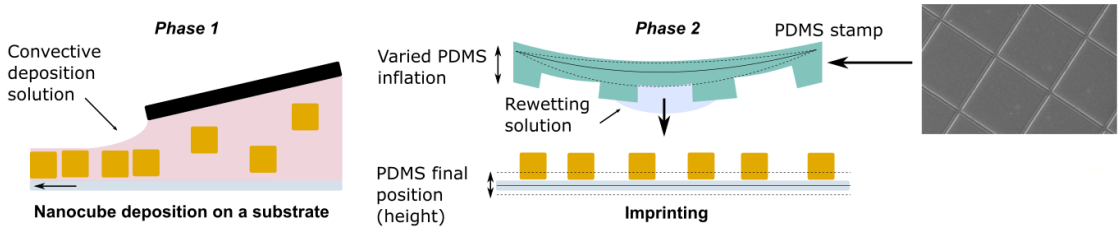

Figure 1: Summary of nanocube assembly using a commercial NIL setup. In phase 1, nanocubes are deposited on a substrate using convective deposition in 1 mM SDS. In phase 2, nanocubes are imprinted by pressing the inflated nanopattern PDMS stamp on the substrate. In order to rewet nanocubes, a droplet of solution is placed on PDMS, we typically use 0.01 wt% Triton X-45 in ethanol. Final PDMS position (height) and PDMS inflation are tuned to control the force exerted on the substrate.

A broad set of experimental conditions were tested to assess the impact of printing parameters, nanocube surface chemistry, deposition methods and ink composition. It is found that reducing the imprinting speed to the minimum (0.4 mm·s^{-1}) and using 0.01 wt% of Triton-X45 in ethanol to wet the nanocubes in phase 2 gave the best results. Triton-X45 appears to promote nanocube mobility, possibly due to favorable interaction with the nanocubes themselves or their capping ligands. Importantly, it is shown that the method is robust and mostly dependent on ink composition, rather than on mechanical parameters such as inflating pressure and PDMS final position (Figure S2). In particular, the presence of PVP was found to be key for nanocube mobility, in line with previous report,[16] but we cannot exclude the existence of other effective ligands. First tests performed with CTAC capped Au nanocubes revealed the need to exchange ligands to PVP to attain adequate nanocube mobility and high yield assembly (Figures S2 and S3). In addition, excess PVP should be present in the deposition solution. This evidences that material composition does not play any major role on the assembly process, as expected, and that this process can be applied to other nanocube materials.

This was confirmed by a systematic series of experiments in which Ag nanocubes were deposited from solutions containing an increasing amount of PVP (phase 1), with the ob-

jective to tune the thickness of the PVP layer underneath the nanocubes (Figure 2). No assembly could be observed in the absence of PVP. Grid patterns started to appear for samples prepared from colloidal solutions with a PVP concentration of 0.125 mg/mL, and high-quality grid patterns were obtained if the concentration was increased to 2 mg/mL (Figure 2d). These findings prompted us to investigate in deeper details how PVP impacts nanocube mobility, as shall be discussed in the following section.

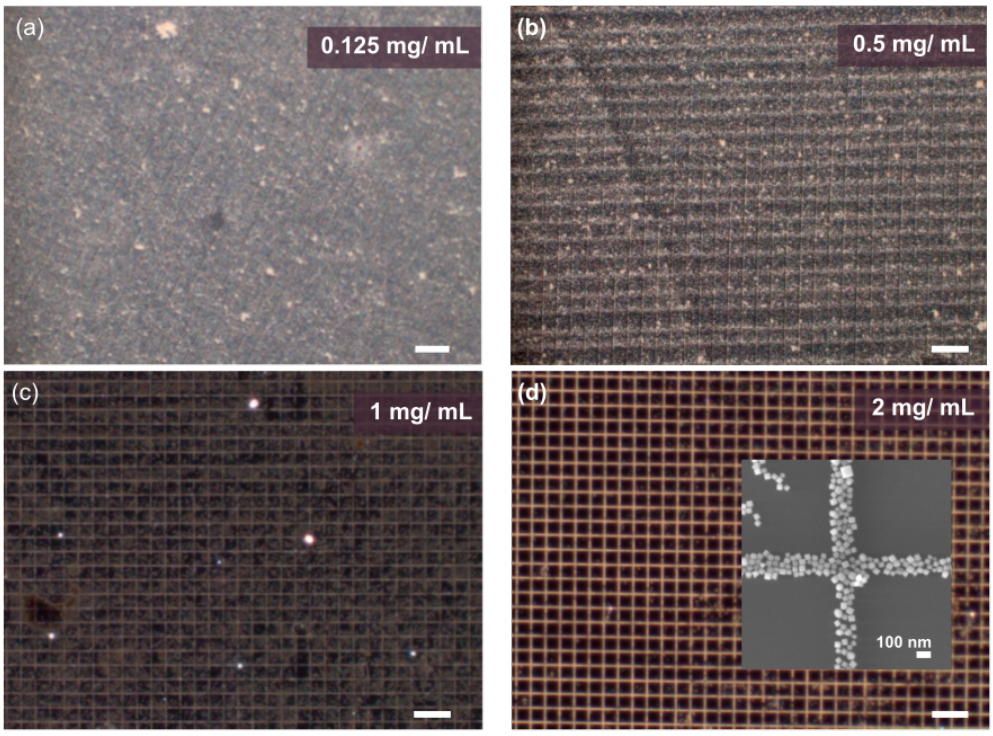

Figure 2: 35 nm PVP-capped Ag nanocubes deposited on glass by convective deposition in SDS with different PVP concentrations and imprinted at 0.4 mm/s, upon rewetting the substrate with 3 μL of Triton-X45 0.01 wt% in ethanol, showing the crucial role of PVP as additive to the convective assembly solution a) 0.125 mg/mL PVP b) 0.5 mg/mL PVP c) 1 mg/mL PVP d) 2 mg/mL PVP in the deposition solution. Inset shows the corresponding SEM image. Scale bars are 1 μm unless states otherwise.

Gap-plasmon spectroscopy ruler

Understanding the key role played by PVP is crucial to propose a sample preparation method to achieve high-quality assembly, independently of the starting material.

As mentioned above, the presence of PVP during nanocube deposition (phase 1) is key for nanocube mobility during nanoimprint (phase 2), whereas its effect is negligible if PVP is introduced only after. On the other hand, nanocubes are pushed away from the nanopatterned area if an excessive amount of PVP is introduced in between them and the substrate. An optimal PVP thickness is therefore needed between the nanocubes and the substrate, but its quantification is challenging. It cannot be calculated from PVP concentration in the deposition solution because convective assembly is a highly dynamic process in which drying forces push the nanocubes against the substrate, altering the local concentration. Standard characterization techniques such as ellipsometry, or AFM are not suitable either, and using TEM to analyze FIB cross-sections is complex, tedious and provides with limited statistical and spatial information. To overcome this issue, we investigated the use of gap-plasmon resonators in the configuration of a patch antenna, that are able to tightly confine light in the nanocavity formed between two parallel conducting surfaces separated by a dielectric spacer [51]. Gap-plasmon resonances are optical modes (Figure 3b) that are extremely sensitive to the dielectric environment, the characteristics of the metal objects (size, shape, material) and the nanogap size. They have been used in previous works as rulers with Angstrom resolution[52,53]. In addition, they have a strong extinction cross-section, so they can be probed with far-field techniques even on the scale of individual objects, making this an ideal platform to perform metrology studies.

We take advantage of gap-plasmon resonances supported in the cavity formed between the flat surfaces of 40 nm Ag nanocubes and a silver mirror, to access information about the thickness of the PVP layer trapped in the gap, with sub-nanometer resolution. The silver mirror is covered by a 0.8 nm-thick Al_2O_3 layer grown by Atomic Layer Deposition (ALD) before nanocube deposition (Figure 3c). In addition to protect the film, the Al_2O_3 layer, acting as a dielectric spacer, enables to set a minimum cavity thickness of 0.8 nm for samples prepared in the absence of PVP, that will serve as references to validate Boundary Element Method (BEM) simulation models and estimate thickness accurately.

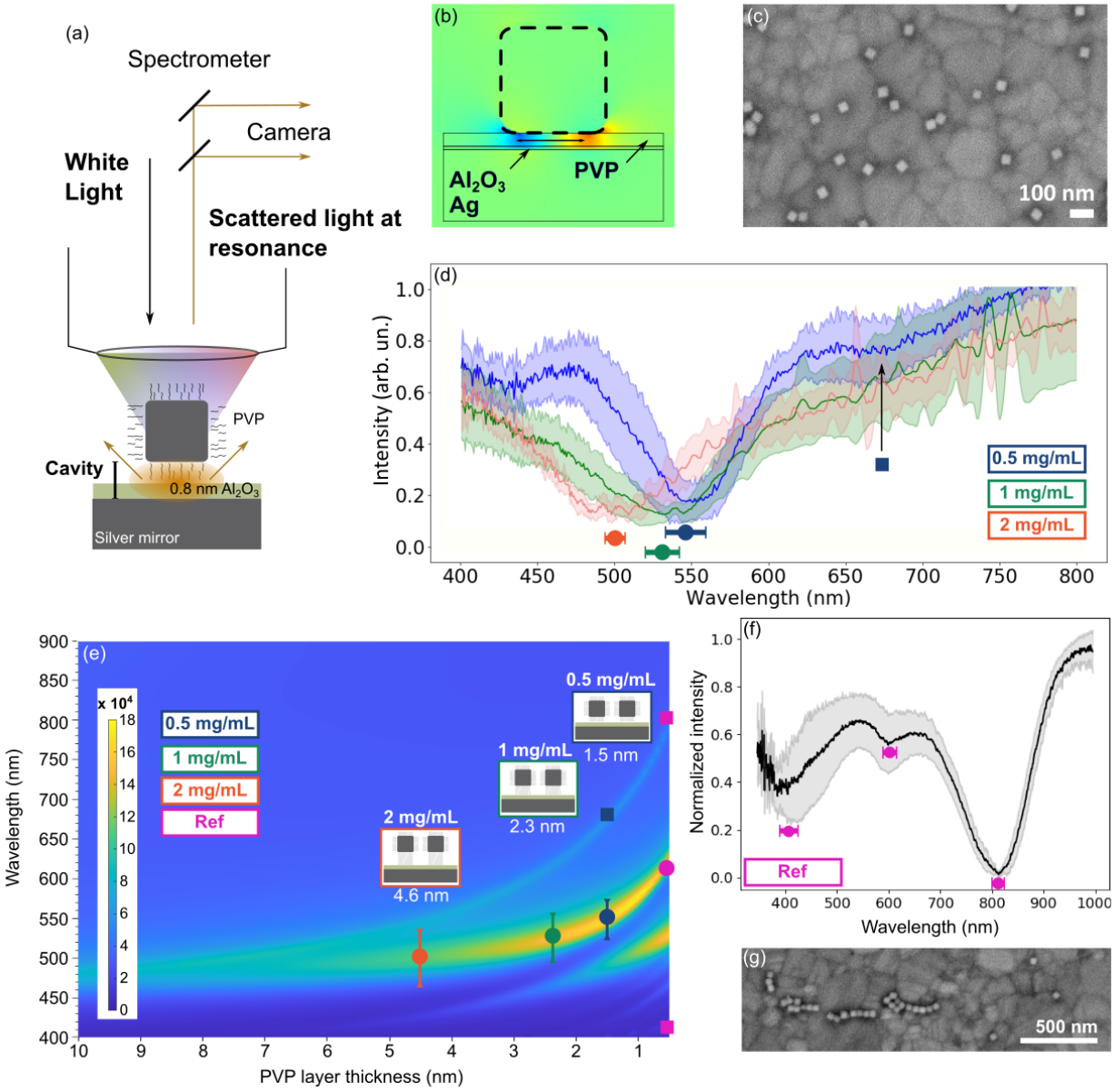

Figure 3: Probing PVP layer thickness using cavity plasmon resonances. a) Schematic representation of the optical setup used to probe gap-plasmon resonances. b) Electromagnetic field distribution (Ez) in a dielectric cavity formed between a silver mirror and a silver nanocube separated by 1 nm Al_2O_3 and 5 nm PVP (simulation performed on Lumerical (FDTD)). c) SEM image of 40 nm Ag nanocubes deposited from a 0.5 mg/mL PVP solution on a Al_2O_3-silver substrate. d) Averaged spectra for 0.5 mg/mL, 1 and 2 mg/mL PVP before nanoimprint. Filled regions show standard deviations between measurements (more than 50 spectra) for each sample at each wavelength. Points and bars indicate mean resonance values as well as standard deviations calculated by fitting each individual spectra with a Lorentzian function.

Figure 3: e) Extinction cross-section (nm^2) map at 65° excitation for various PVP thickness. Points and bars correspond to the mean experimental cavity plasmon resonances (same as d) and mean peak widths for the three samples (0.5, 1 and 2 mg/mL), obtained by fitting spectra with a Lorentzian function around 500-550 nm. For the 0.5 mg/mL sample, a blue square indicates the position of the long wavelength mode. Resonances from the reference sample shown in (f) are indicated in pink. f) Reference sample realized by LB and corresponding averaged spectra for 10 different 20× BF measurements. Shadow areas represent standard deviations calculated for each point, dots indicate the average resonance values obtained by fitting each spectrum with a Lorentzian function, and bars the corresponding standard deviations g) Corresponding SEM image.

Nanocubes deposited on silver-Al_2O_3 samples from solutions containing 0.5, 1 and 2 mg/mL PVP were probed with a home-made micro-spectroscopy setup (see Figure 3a) in bright field (BF) with 20×, 50×, and 100× objectives. To assess the homogeneity of the deposition, spectra are taken in four different zones called Z1-Z4 (roughly 50 measurements each) along the deposition direction (Figure S4). Figure 3d show spectra averaged over the whole samples together with statistics (mean values and standard deviations), all magnifications combined, while details for each zone can be found in SI (Figures S5 and S6).

As the amount of PVP in the deposition solution is increased from 0.5 to 2 mg/mL a blue-shift as large as 50 nm is observed. This results from the increase in the cavity thickness due to the larger amount of PVP trapped between nanocubes and substrate (Figure 3d).

In order to quantify PVP thickness, we performed electromagnetic simulations. Light can be coupled to different modes, depending on the resonator geometry and the excitation wave vector. The fundamental mode (s_{11}), easily excited at normal illumination, typically lies in the near infrared for small gaps. Higher order modes are observed at shorter wavelengths and some of them, such as the hybrid s_{02}, can only be excited at an angle.[54]

Our experimental setup allows excitation of all these modes due to the large numerical aperture of the objectives (0.4 to 0.9), although the extinction cross-section will vary. Figure 3e presents the simulated extinction cross-section of individual gap-plasmon resonators as a function of PVP thickness at 65° illumination, that corresponds to the largest numerical aperture used to collect the spectra. The figure shows that this method is extremely sensitive,

especially for ultrathin layers. As the PVP layer increases, the fundamental mode merges with higher order modes yielding broader peaks, in agreement with experimental data (Figure 3e). The apparent discrepancy in relative cross-section between experiments and simulations is most likely due to the latter being computed at a fixed large angle for a single nanocube as opposed to being integrated over all angles collected by the objective on the sampled area with multiple nanocubes (Figures S9 and S10).

Resonance positions being greatly affected by nanoparticles shape and size, as well as the different layers thicknesses and optical indices, we performed statistics on nanocube geometry by measuring size and bending radius of 25 nanocubes from TEM images (Figure S7), and characterized the Al_2O_3 layer using ellipsometry measurements as well as X-ray reflectivity measurements in order to assess its thickness and dielectric constant (Figure S8).

Due to the extreme sensitivity of this technique, it also appeared important to validate the model on a reference sample without PVP. Two different routes were explored (i) deposition of floating nanocubes from a Langmuir Blodgett (LB) trough filled with a Sodium Borohydride ($NaBH_4$) solution (known to generate ligand desorption from nanoparticle surfaces[55]), which resulted in nanocube assembly in clusters and chains (Figure 3g) and (ii) dropcasting nanocubes from a $NaBH_4$ solution, which resulted in the deposition of individual nanoparticles (Figure S10).

Both reference samples gave similar responses, with resonances around $\lambda = 800$, 600 and 400 nm (Figures 3f, S9 and S10). This indicates that the gap size of aggregated nanocubes can be estimated by extrapolating simulation results obtained for individual nanocubes. Comparison between simulated cavity plasmon resonances and experimental results of reference samples suggests that the amount of residual PVP in reference samples is ~ 0.6 nm (Figures 3e), although non-local simulations would be needed for better precision. We consider that a good match between simulation results and experimental data is obtained in terms of resonance wavelength, enabling us to use the thickness of the PVP layer as the only free parameter in the model.

Next, we used this model to quantify the thickness of the PVP layer for samples deposited with different amounts of PVP. With the assumption of a constant PVP refractive index of 1.53, we estimated a thickness of ∼1.5 nm for 0.5 mg/mL, ∼2.3 nm for 1 mg/mL and ∼4.6 nm for 2 mg/mL samples using mean resonance values (Figure 3d and e). Note that even at 0.5 mg/mL the concentration of free PVP is larger than the critical concentration ensuring complete coverage of the nanocube facets.[56] As a consequence, we expect that the refractive index used in the simulation does not change considerably.

Nanoimprint lithography was applied to these samples to confirm the key role of the PVP layer. No grid assembly was observed when the nanocube-Al_2O_3 distance was 1.5 and 2.3 nm, with no mobility for the former and some limited nanocube mobility for the latter (Figures 4a and b). However, almost continuous grids were obtained after imprint lithography for samples in which the nanocube-substrate distance was in the order of 4.6 nm (Figure 4c). These observations indicate the existence of a PVP thickness threshold beyond which nanocubes have enough mobility to reach the trenches in the nanopattern, regardless of their initial position. This will be further analyzed in the next section.

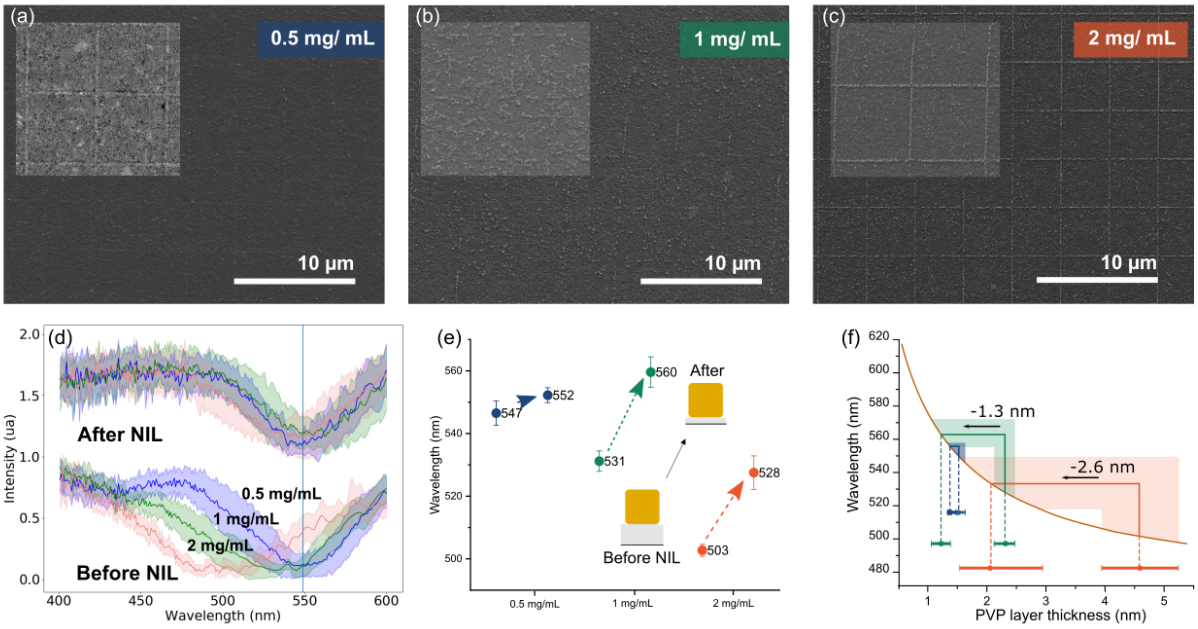

Figure 4: Impact of PVP layer thickness on nanocube mobility. Sample 1 (a), 2 (b) and 3 (c) are imprinted upon rewetting the substrate with 3 μL of Triton-X45 0.01 wt% in ethanol; d) Averaged spectra for the 3 samples 0.5 mg/mL, 1 and 2 mg/mL PVP before (bottom) and after (top) imprinting. Filled regions show standard deviations between measurements (more than 50 spectra) for each sample e) Cavity plasmon resonances mean values (circles) and standard deviations (bars) obtained by fitting each spectrum with a Lorentzian function and confronted to values obtained prior to imprinting f) Variation in PVP thickness estimated by confronting values from (e) to the simulations, taking into account standard deviations.

After nanoimprint lithography the cavity resonance was probed again, approximately in the same zones (optical images of the different zones can be found in Figure S11), and exhibited a notable red-shift. This is illustrated in Figures 4d and f, that compare the evolution of the resonance positions averaged over all zones. These results correspond to a narrowing of the PVP layer from 4.6 to 2 nm (2 mg/mL sample) and from 2.3 to 1.2 nm (1 mg/mL sample) (Figure 4f). Interestingly, for the 0.5 mg/mL sample, on which nanocubes had no mobility, the cavity plasmon resonances remained unchanged, while averaged spectra of samples 1 and 2 mg/mL are significantly red shifted, resulting in a lower difference between the three samples upon imprinting (Figure 4d). In addition, a maximum value of 570 nm, corresponding to a PVP layer of roughly 1 nm, is never exceeded (Figure S12). These observations suggest that the PVP layer narrows as a result of nanocubes motion, and once a

critical thickness ($\sim$ 1 nm) is reached, mobility is suppressed. Interestingly, we do not observe the signature of coupling between adjacent nanocubes neither before or after nanoimprint, possibly because of averaging among many different coupling conditions which result in an obvious resonance broadening compared to that of individual gap-plasmon resonators.[57]

We do not observe any noticeable trend in terms of resonance shift after nanoimprint over different zones, suggesting that nanocubes outside nanopatterned areas are also displaced (Figures S11, S12).

In our configuration, most of PVP chains are probably only weakly trapped between nanocubes and the substrate. Therefore, we hypothesize that as nanocubes are displaced, the average PVP thickness underneath decreases as a result of VDW interactions and its dissolution in the rewetting solvent, until mobility is no longer possible due to larger friction (see next). Although this appears to limit nanoparticles mobility to a few μm, it is sufficient for nanocubes to reach the nanopattern trenches and remain trapped, as solvent and excess PVP are squeezed out of the assembly area.

Mechanics of nanocube assembly

We attempted to identify the different forces acting on the nanocubes during nanoimprint to shine light on the mechanism responsible for their displacement from their initial positions to the trenches. Dominant interactions between uncharged nanoparticles are electrostatic VDW forces, which are very sensitive to the separation distance between the two objects. In the case of two parallel planar surfaces of size l, separated by a distance d, the interaction force is perpendicular to the substrate and can be written as:[58]

$$F_{VDW} = \frac{A_{HAM}}{6\pi d^3} l^2$$

Where A_{HAM} is the Hamaker constant, that takes into account geometrical and material parameters.

This force, responsible for binding the nanocubes to the substrate, rapidly decays with separation with a $1/d^3$ dependence. Importantly, a 30-fold reduction in VDW forces is obtained if the nanocube-substrate distance is increased from 1.5 to 4.5 nm, independently of the Hamaker constant value. When nanocube-substrate distance is further increased by introducing higher amount of PVP in the deposition solution (5 mg/mL), we observed that nanocubes can be detached from the substrate simply by the introduction of some solvent (data not shown), confirming the key role of the VDW interaction.

To initiate lateral motion of the nanocubes an energy barrier has to be overcome. It can be related to adhesion and friction forces (F_F). Polymer brushes, either bonded or adsorbed to the substrate, have the ability to retain solvent and maintain a liquid interfacial layer even under compression, reducing friction through lubrication. Additionally, repulsive steric interactions between polymer chains mitigate adhesion forces between surfaces.[59,60]

Friction forces are related to the force perpendicular to the substrate (that in our case is the VDW force (F_{VDW})) via the static friction coefficient ($0<\mu<1$):

$$F_F = \mu \; F_{VDW} \tag{1}$$

Considering that PVP is soluble in the solution used for rewetting nanocubes during imprinting, we assume that adhesion forces are negligible, and that the friction coefficient is low (<0.5).[60] For simplicity, F_{VDW} is calculated by considering silver nanocubes interacting with the silver film, omitting the Al_2O_3 layer, and by assuming that during assembly the two surfaces are separated by water, corresponding to $A_{HAM}=1\cdot10^{-19}$ J (see SI *Models and calculations*).[61] The horizontal force required to initiate nanocubes motion is shown in Figure 5a for different friction coefficients as a function of the nanocube-substrate distance (solid lines). Black dots representing the three experimental conditions have been added at the corresponding nanocube-surface distance, whereas the vertical position has been chosen arbitrarily to be at $\mu=0.25$ for an easier visualization of the graph.

Another aspect worth discussing concerns the (horizontal) force pushing the nanocubes towards the trenches. As the nanopatterned stamp approaches the substrate, the liquid introduced to rewet the sample spreads and is squeezed out of the impression area. We hypothesize that this liquid flow exerts a Stokes drag on the nanocubes and is responsible for their motion (Figure 5b). This drag force can be written as:

$$F_D = 3\ \pi\ \eta\ v\ d_v\ K \tag{2}$$

where η is the solvent viscosity, v the solvent escaping velocity, d_v the diameter of a sphere with a volume equal to that of the nanocubes (volume equivalent diameter) and K a shape factor.

To test this hypothesis, a simplified model is developed to estimate the fluid velocity, that depends on the speed at which the mold is pressed on the substrate, on geometrical parameters of the mold, and on the distance from the substrate (Figure S13). This enabled to estimate the order of magnitude of this drag force at intermediate positions and at its limit value (just before touching the nanocubes) and to compare it with F_{VDW}, as illustrated in Figure 5a (dashed orange lines). It is therefore possible to consider that the lateral forces exerted by the escaping solvent are enough to induce nanocube mobility if the PVP thickness is beyond a certain threshold value. Below a certain PVP thickness threshold however, the Stokes drag can no longer balance the friction force nanocube-substrate due to increased VDW attraction (Figure 5c). The force required to initiate nanocube motion is thus almost in quantitative agreement with the Stokes drag acting on their surface.

This is in accordance with a previous report from Agrawal *et al.*, showing that control experiments performed in the absence of solvent yielded no assembly, even in the presence of a suitable nanocube-substrate distance. In addition, PVP needs to be soluble in the solvent used to rewet nanocubes, otherwise the assumption that adhesion forces are negligible would no longer be valid and the force required to initiate motion would be substantially higher,

necessitating for a larger Stokes drag. Note that the Stokes drag can be tuned with the assembly parameters, but also by increasing solvent viscosity.

The minimum required force is a necessary but not sufficient condition to achieve good assembly. In fact, after motion is initiated, nanocubes have to reach the trenches before contact with the bottom surface of the PDMS stamp, setting further restrictions on the optimal ink composition. This is illustrated in Figure 5a by showing the magnitude of the drag force for various distances and the approximate time before contact is achieved (orange dashed lines). Note that this simplified model does not take into account non-linear phenomena such as the non-Newtonian properties of the fluid, or the non-linear dependence of nanocube-substrate friction as a function of the contact load, which may be relevant during nanocube motion.

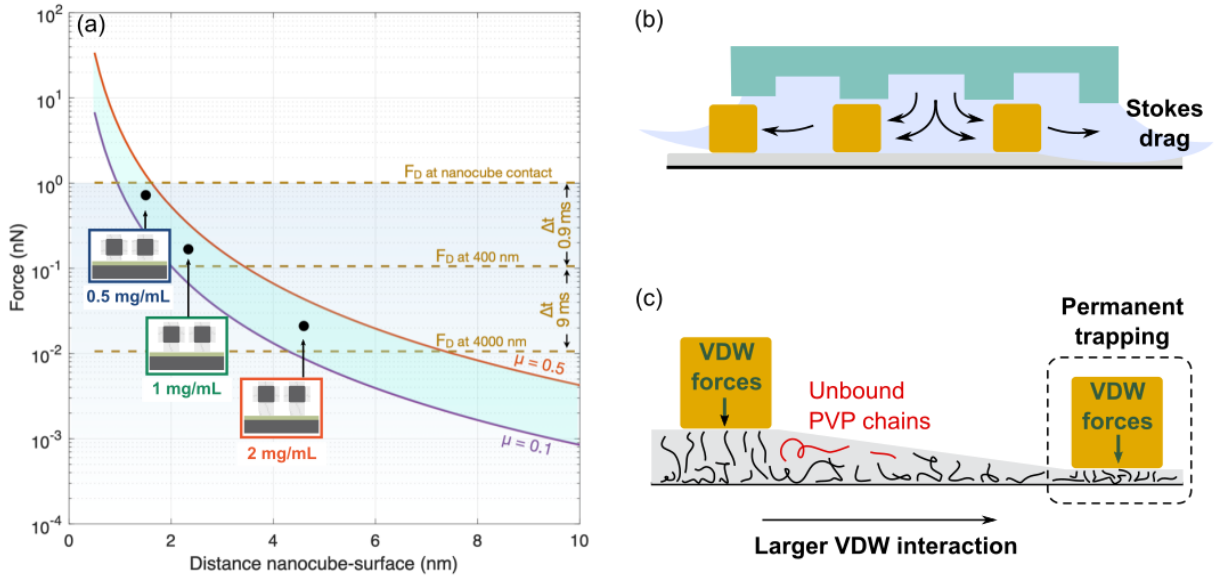

Figure 5: NIL mechanism summary. a) Force required to overcome nanocube-substrate interaction and displace nanocubes plotted for different friction coefficient (μ) with respect to the approximative Stokes force exerted on nanocubes by solvent b) Schematic representation of solvent squeezed out of the substrate and exerting increasing lateral forces on nanocubes as well as dissolving part of PVP chains c) Nanocubes gradually loosing their PVP spacer layer as they are displaced on the substrate as a result from VDW attraction and PVP chains solubility in the rewetting solvent, which eventually results on permanent trapping.

Operando experiments performed by mounting the NIL setup on top of an inverted optical microscope confirmed that assembly took place as the PDMS stamp was pressed on the substrate and not at a later stage upon solvent evaporation. As a result, temperature control is not necessary for good quality assembly, however nanocubes should be dry before retracting the stamp to avoid disruption of the assembly. Unfortunately, no video could be recorded due to difficulty in maintaining focus when PDMS was pressed over the substrate.

Our interpretation of the mechanism is consistent with another set of experiments in which PVP was added on top of samples prepared with varied nanocube-substrate distances (tuned by varying the amount of PVP added to the deposition solution in phase 1). Whereas nanoparticle mobility did not improve in the absence of a PVP spacer layer (nanocubes in contact with the substrate), for larger separations, we observed a substantial increase in the assembly yield, as illustrated in Figure S14, if a considerable amount of PVP was deposited thereafter (10 μL of 1 mM PVP in ethanol). The introduction of PVP in a second stage improves the resilience of the PVP layer during nanocube motion (likely slowing down its thinning) and increases the viscosity of the solution, with a direct impact on the drag force. This enabled assembly of nanocubes deposited with 0.125 mg/mL PVP on glass substrates (Figure S14a), that could not be achieved before (see Figure 2a).

Large scale printable nanogrids

A good understanding of the mechanism enabled to further optimize printing parameters. First of all, the PVP layer between nanocubes and substrate should be maximized while making sure that the nanocubes remain bounded to the substrate.

Different particle types, but also different synthesis batches of the same nanoparticles, might present different amounts of PVP on their surfaces. Furthermore, different substrates have different VDW interaction magnitudes with nanoparticles, as accounted for by the Hamaker constant. As a result, the amount of PVP needed for optimal mobility should be

optimized for every nanoparticle-substrate couple.

A good empirical method to determine the maximum allowed amount of PVP is to gradually increase its concentration in the deposition solution ensuring that nanocubes are not dissolved by introducing a droplet of ethanol. An optimal PVP concentration of 1 mg/mL for 40 nm Ag nanocubes is determined on glass, instead of 2 mg/mL on Al_2O_3 (see Figure 6a to c). 35 nm Au nanocubes required lower amount of excess PVP (0.5 mg/mL), presumably as a result of a larger adsorbed PVP from ligand exchange (Figure 6d).

The procedure was repeated with a 25 cm^2 commercial NIL setup, allowing for larger PDMS deformation and extensive parameter control (Figure S15c). A new master was prepared, composed of 9 1×1 mm^2 grids of varied pitch and width, with constant trenches depth of 40 nm (Figure S16). Large scale homogeneous assemblies were obtained for both Ag and Au with different grid geometries, without needing to optimize printing parameters (Figure 6), except for nanocube density on the substrate to produce close packed continuous grids without excess nanocubes. This highlights the major role played by the ink composition. It is worth noticing that the printing area is only limited by the Si master used to fabricate the PDMS mold. We expect that this process could be scaled up to an arbitrarily large area.

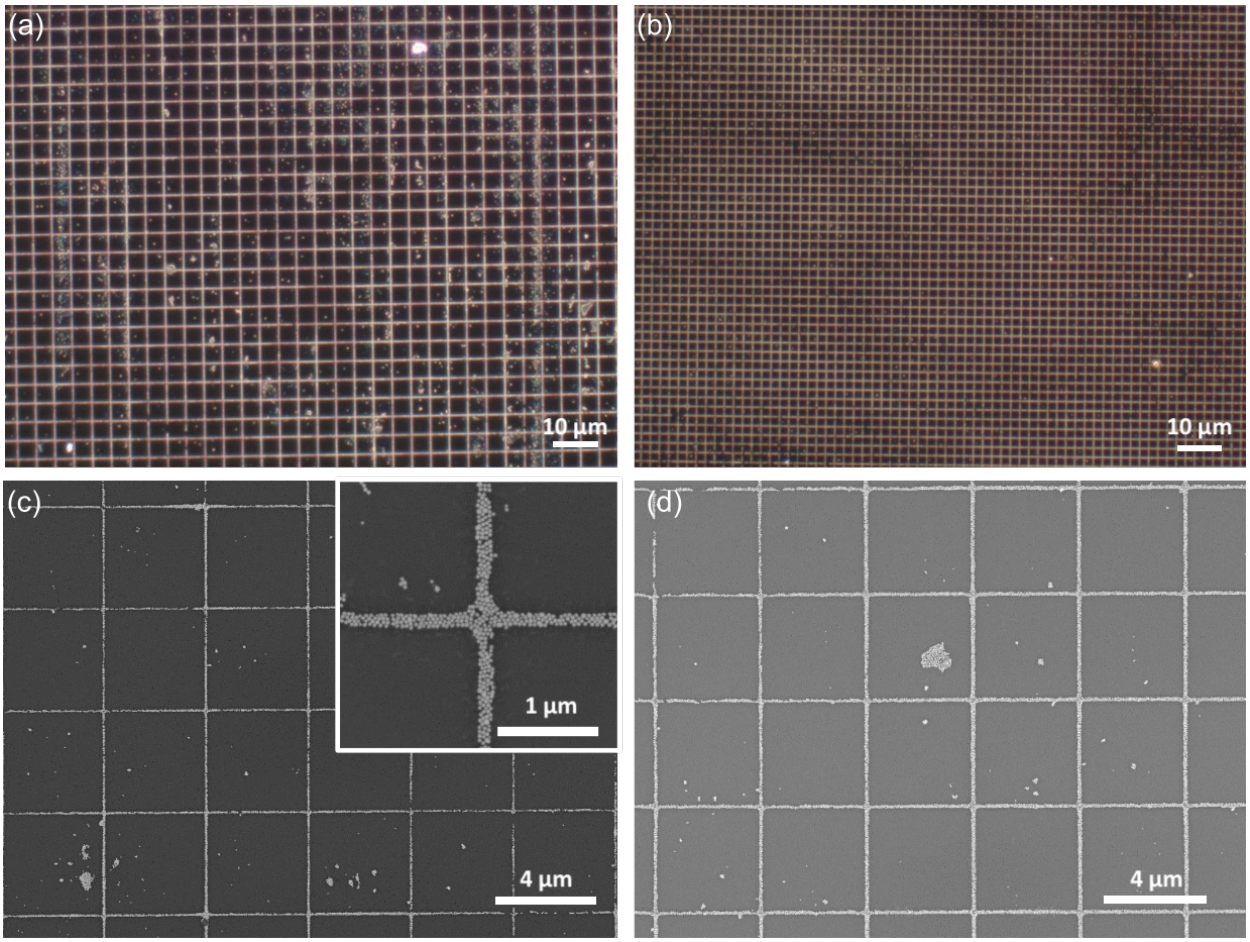

Figure 6: Optical images of a) Ag grid with 4 μm pitch b) Ag grid with 2 μm pitch. SEM images of c) Ag grid with 4 μm pitch d) Au grid with 4 μm pitch. Ag and Au were deposited by convective assembly in 1 mM SDS in the presence of 1 mg/mL and 0.5 mg/mL PVP respectively (imprinting parameters described in the Methods section).

Finally, such grids could be transferred from glass to PDMS by curing PDMS on top and peeling it off (Figure 7a). Such flexible assemblies could be the starting point for nanocube epitaxy, discussed elsewhere, to obtain continuous grids.[11,12] This has the potential to spark major interest in the field of flexible electronics.

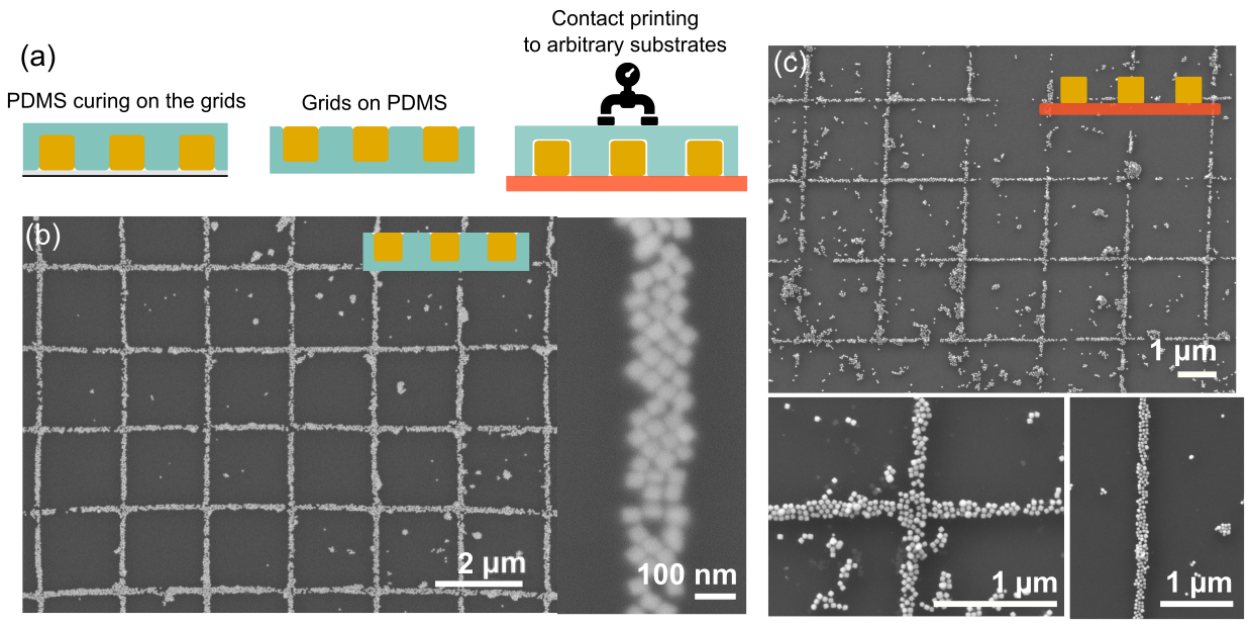

Figure 7: a) Schematic of the process, from curing liquid PDMS on top of nanocubes to peeling PDMS off and deposition on a new substrate by contact printing b) SEM images of grids in PDMS. Inset on the bottom left shows the flexibility of the PDMS substrate supporting the grids. c) Grids deposited on silicon upon contact printing.

Furthermore, thanks to PDMS low surface energy, assemblies can then be printed to virtually any substrate. Figure 7c shows the transfer of the grid from PDMS to silicon. This is of paramount importance for integration in optoelectronic devices. Although at the current stage transfer to a new substrate is sub-optimal, we believe that the process can be dramatically improved if nanocubes are welded together and constitute a continuous material. Employing larger nanocubes or using intermediate sacrificial materials such as PMMA could be an alternative to ameliorate the transfer process.

Finally, we tested the optimal ink composition with a home-made setup to demonstrate the generality of the approach. Details of the setup can be found elsewhere[16] or in Figure S17. Face-to-face assembly of 35 nm Au nanocubes could be achieved, as presented in Figure S18. We observed, however, a lower degree of reproducibility.

We hypothesize that nanocube face-to-face assembly along PDMS trenches originates from PDMS and substrate unavoidable slight misalignment, generating "sliding" effects as

PDMS is pressed against substrates, forcing nanocubes to orientate with the trenches edge (Figures S18, S19). Conversely, with commercial NIL setups nanocubes are typically not assembled face-to-face (Figure 6). Therefore, the introduction of a subtle sliding between the PDMS mold and the substrate could lead to a face-to-face assembly even when using soft-contact NIL setups as the ones used here (Figure S20).

Conclusions

It has been demonstrated that nanoparticle imprint lithography can be downscaled to 35-40 nm nanocubes for two different metals (Ag, Au). Conformal contact between the nanopatterned mold and the substrate allowed to achieve reproducible assembly and to gain valuable insights. We propose a quantitative description of the mechanism by analyzing the different forces at play and comparing them to experimental results. We probe via gap-plasmon spectroscopy the nanocube-substrate distance with sub-nanometer resolution, revealing that its careful tuning is key to balance VDW interactions and the Stokes drag acting on the nanocubes in the imprinting phase. Although some of our findings may be specific to nanocubes, the methodology can benefit the whole nanoparticle-based imprint lithography domain, as we provide with quantitative evidence on the role played by the distance and ligands on the nanoparticle mobility. These insights set a solid framework for future research on nanoparticle imprint lithography for the fabrication of high quality metal nanopatterns on a large area. mm^2 printable metal nanogrids with a variety of widths and pitches were obtained, with limited sensitivity to the imprinting conditions or the setup used, showing that the method is robust and the ink composition is the most critical parameter. The simple deposition procedure used could be applied to different types of nanoparticle material or geometry. In fact, PVP is commonly used in the synthesis of various metal, metal oxide

and chalcogenide nanoparticles,[62] which makes this technique highly versatile. PVP could in principle be replaced by other soft lubricating compounds for specific applications, while the force applied to displace nanocubes, originating from solvent lateral motion, could be tailored by tuning solvent viscosity using additives, allowing to envision the implementation of this method to a variety of nanoparticles. In addition, the formation of a spacing layer can be decoupled from the deposition of nanoparticles and enables for additional control of the optimal nanoparticle density on the substrate, that is critical to obtain close packed assembly over large scale before being processed into a continuous solid material via nanocube epitaxy or thermal methods. The results presented in this work will help imprint lithography to become a game changer in the fabrication of compact nanoparticle assembly that can be integrated as printable metasurfaces or transparent electrodes in flexible optical and electronic devices.

Methods

Material

PDMS was purchased from Wacker (RT601), $HAuCl_4$, HNO_3, NaBr, NaCl, CF_3COOAg, NaSH, HCl, Ethylene Glycol, PVP (55,000 Mw) and $NaBH_4$ were purchased from Merck at the highest purity available. Trimethylaluminium (TMA) was purchased from Strem Chemicals (98%). Deionized water (18.2 MΩ·cm) was taken from a Milli-Q Direct 8 system (Merck).

Nanocube synthesis

Silver Nanocubes synthesis

40 nm Ag nanocubes were synthesized following a procedure from Xia's group.[63] Briefly, 25 mL of ethylene glycol was pre-heated in a round-bottom flask using a 155°C oil bath at a stirring speed of 200 rpm. 300 μL of 3 mM NaSH was then added to the solution. After 2 min, 2.5 mL of HCl 3 mM and 6.25 mL of 20 mg/mL PVP were quickly added. After another 2 min, 2 mL CF_3COOAg 282 mM was added to the round bottom flask. Reaction was finally quenched using an ice-cold water bath after 1H30. Nanocubes were washed twice by centrifugation and redispersed in ultrapure water at a concentration of roughly $2{\cdot}10^{14}$ nanocubes/mL (Figure S21).

Gold Nanocubes synthesis

40 nm gold nanocubes were synthesized following Park *et al.* procedure.[64] Briefly, 10 nm CTAC-capped seeds were overgrown in a 50 mL round bottom flask using 6 mL of 100 mM

CTAC, 30 μL of sodium bromide at 40 mM, 100 μL of the 10 nm seed solution at 2 OD in 20 mM CTAC, 390 μL 10 mM ascorbic acid and 6 mL of 0.5 mM $HAuCl_4$ solution. The solution was left to react for 25 minutes at RT with gentle stirring prior to centrifugation. The nanocube solution was washed twice and redispersed in 10 mL of ultrapure water at a concentration of roughly $2{\cdot}10^{14}$ nanocubes/mL (Figure S22).

Master fabrication

The first silicon master (Figure S1) was fabricated with e-beam lithography using a hydrogen silsesquioxane (HSQ) resist, deposited by spin coating to form a 40 nm film. After exposure, unexposed resist was washed away using TMAH (50°C, 60s), leaving behind the grid patterns with no need for further etching steps.

The second silicon master (Figure S16) was realized by e-beam lithography using PMMA resist on silicon. Upon exposition and development, a thin layer of chrome was evaporated on the substrate to be used as a hardmask. PMMA was then lifted-off in acetone. Silicon was then etched by 40 nm using Reactive Ion Etching (RIE). Chrome was finally removed using a commercial chrome etchant.

Masters were then silanized with 1H,1H,2H,2H-Perfluorooctyltriethoxysilane and perfluorodecyltrichlorosilane in a vacuum oven and desiccator respectively upon plasma treatment to ease PDMS demolding.

Silicon masters were replicated to PDMS. For integration in commercial setups, commercial PDMS (monomer and polymerizing agent mixed in a 9:1 ratio) was cured directly on special stamps adaptable to the NIL setups printing heads and enabling for PDMS inflation. For the homemade NIL setup, PDMS stamps were prepared on a glass slide (Figure S17). Upon reticulation of PDMS (80°C, 24H) the PDMS template was peeled off from the silicon master.

Substrate preparation (phase 1)

Au nanocubes were deposited upon ligand exchange from CTAC to PVP following Fan *et al.* procedure (modified).[65] Roughly 100 μL of 50 mg/mL PVP (Mw 55000 g.mol^{-1}) in water and 3 mL ethanol were added to 1 mL of 10^{12} nanocubes/mL CTAC capped Au nanocubes stock solution. The solution was stirred for about 48H at RT before centrifuging nanocubes twice (9000 rpm, 10 minutes) in order to remove the excess PVP completely.

PVP capped Au and Ag nanocubes were then redispersed in SDS 1 mM with varied PVP concentrations (0.125 - 2 mg/mL), at a concentration of roughly $4{\cdot}10^{14}$ nanocubes/mL for silver and 10^{13} nanocubes/mL for gold.

Samples were prepared using convective assembly in SDS 1 mM on hard substrates (typically glass). Briefly, the colloidal solutions (20 μL) were dragged with a glass slide fixed 100 μm above the PDMS substrate using in a home-made system. Convective assembly was performed between 30 and 40°C with a speed between 3 and 5 μm$\cdot$s^{-1}. This enabled to achieve nanocube density close to the optimal (roughly 100 nanocubes per μm^2, Figure S23).

Imprinting (phase 2)

Commercial set-ups

Nanocube Imprint Lithography was implemented on the micro-contact-printing process machines μCP Core and μCP4 by GeSIM-Germany (Figure S15). Briefly, the nanopatterned PDMS stamps are situated on a printer head moving in the z-direction at controlled speed and substrates are placed on a heating plate. Finally, the PDMS molds are inflated using air pressure. Typical working parameters were an air pressure of 250 kPa and a printing speed of 0.4 mm/s for the μCP Core system and an air pressure of 10 kPa and an printing speed of 0.1 mm/s for the μCP4 system. Contact positions were defined at a distance of 25.7 mm and

25.5 mm respectively from the PDMS stamp original position unless mentioned otherwise. These values depend on the setup used and the substrate thickness.

Homemade set-up

The homemade set-up developed by Agrawal *et al.*[16] was mounted on a Universal Testing System model 5965 with 50 kN force capacity from INSTRON (Figure S17). A flat nanopatterned PDMS stamp was placed at the top clamp and the samples were placed at the bottom clamp equipped with a Peltier element. Parameters were imprinting speed and load. We typically worked with a speed down of 0.1 mm/min and load of 8N.

Imprinting

In all cases samples were rewetted with a 3 to 5μL droplet of Triton X-45 0.01 wt% in ethanol (deposited on the PDMS stamp). Upon imprinting, the PDMS stamp position was maintained (load was maintained for the home-made set-up) for 30 minutes while increasing the temperature to 55°C. Stamp were finally retracted upon solvent evaporation.

Gap plasmon spectroscopy measurements

Substrates

Preparation

Substrates consisted of a 200 nm thick Ag thin film deposited on a glass slide and capped with 0.8 nm Al_2O_3. Silver was deposited by thermal sputtering on silicon and subsequently peeled off to obtain a flat silver surface. Al_2O_3 was deposited by ALD in Fiji 200 reactor (Veeco-Cambridge Nanotech) at 100°C, using TMA and DI water deionized water as precursors (10 ALD cycles).[66]

Al_2O_3 layer characterization

Samples were characterized by Spectroscopic ellipsometry (J.A Woollam Co, M2000V) and X-Ray reflectivity (Panalytical X'Pert Pro MPD θ-θ) in order to precisely estimate Al_2O_3 thickness and dielectric constant. We measured optical indices and thickness on Al_2O_3 layers of increased thickness (10 to 100 ALD cycles) deposited both on silver and silicon and concluded that thickness indeed increased linearly with the number of ALD cycles and estimated the Al_2O_3 layer (Figure S8). The refractive index dispersion was measured on a 10 nm thick Al_2O_3 deposited on silicon.

Reference samples

Two reference samples were prepared. First, 50μL of 40 nm Ag nanocubes stock solution was centrifuged 3 times (11000 rpm, 10 minutes), redispersed twice in ethanol and finally in 50μL CH_3Cl_3. Upon deposition of the nanocube solution on a water subphase in a LB trough, barriers were closed at low speed. Then, 10 mM $NaBH_4$ was introduced as the subphase using a peristaltic pump with a speed of 20 rpm for 15 minutes (roughly 60 mL of solution was exchanged) in an attempt to remove PVP from their surface.[55] Finally, water was introduced again in order to rinse nanocubes, and barriers further closed. Finally, floating nanocubes were transferred from the water-air interface to a glass-silver-Al_2O_3 (0.8 nm) substrate (Figure S9).

A second sample was realized by mixing 100μL of $NaBH_4$ 10 mM with 5 μL of 40 nm Ag nanocubes stock solution in an eppendorf. After 3 minutes, 2 μL of the solution was dropcasted on a glass-silver-Al_2O_3 (0.8 nm) substrate and blow dried after 5 minutes, which resulted in sparse single nanocube deposition (Figure S10).

Main samples

Main samples were realized by depositing nanocubes on silver-Al_2O_3 substrates using convective assembly with different PVP concentration (0.5, 1 and 2 mg/mL). Convective deposition was performed under 40% humidity, at a speed of 5 μm·s^{-1} and a temperature of 30°C for all samples (Figure S4).

Transfer to PDMS and contact printing

Grids could be transferred to PDMS and printed to arbitrary substrate by curing commercial PDMS at 60°C for 24H on Au and Ag grids assembled on glass. Upon peeling PDMS off, the grid patterns detached from the glass substrates and remained on the flexible PDMS.
In a second step, grids could be deposited on a receiving silicon substrate by contact printing. The silicon sample was washed with acetone, IPA, and treated with O_3 for 20 minutes. 10 μL of PVP 200μM in ethanol was deposited on the grid to facilitate printing. Upon ethanol evaporation, excess PVP was rinsed with water.
Finally, 10 μL CH_3Cl_3 was deposited on the silicon substrate maintained at 20°C using a peltier element. The PDMS substrate was then pressed on the receiving substrate. CH_3Cl_3 was let to permeate PDMS at 20°C for 5 minutes before raising the temperature to 50 and then 70°C. The whole process was monitored using an optical microscope by looking through the transparent PDMS, to ensure for good contact between the two substrates and position assembled areas.

Characterization and simulations

Assemblies of nanocubes on non-conductive samples (glass, PDMS) were imaged using a scanning electron microscope (JEOL 7900F) in low vacuum mode with a pressure of 60 Pa. TEM was performed with a JEOL 2100F.

Optical characterization was performed with an inverted microscope (Zeiss Axiovert 200M) with an air objective (100X, NA = 0.9) in reflection. Light was coupled into a 50 μm optical fiber. Spectra were taken in bright field with an integration time of 200 ms for objective x100 (collection spot diameter of $\sim$ 1.3 μm), 100 ms for objective x50 (collection spot of 2.62μm), 50 ms for objective x20 (collection spot of 6.55μm); and in Dark field with integration times of 1000 ms (3200K). Part of the samples were left free of nanocubes and used as the reference to take into account the spectral response of the system.

The commercial software Lumerical was used to simulate the elecromagnetic field enhancement Ez formed in the Al_2O_3-PVP dielectric cavity between a silver mirror and a silver nanocube. Further simulations were performed using the MNPBEM toolbox on Matlab developed by F. J. Garcia de Abajo and A. Howie[67–69] and modified to our parameters. Silver nanocubes were simulated with the dielectric constant from Johnson and Christy using TEM statistics results (nanocube size of 40.5 and bending radius of 8.2 nm, Figure S7). The Al_2O_3 layer was simulated with a thickness of 0.8 nm to match X-Ray Reflectivity and ellipsometry results and experimental data obtained by ellipsometry was used for Al_2O_3 dielectric constant. Finally, a constant index of 1.53 was used to simulate PVP. Simulations were performed for varied PVP thickness under normal and 65° excitation.

Associated content

The Supporting Information is available free of charge. Details of the Si masters, the nanoimprint setups, additional optical and electron microscopy images, details of the sample zones used for gap-plasmon metrology, TEM images, XRR data, additional specroscopy data, details on the fluid mechanics model, nanocube characterisation.

Acknowledgement

The authors thank Eitan Oksenberg for fruitful discussions, Oznur Gulabigul for the gold nanocube synthesis, D. Chaudanson and A. Altié for support with TEM characterisation and F. Bedu for support with e-beam lithography. B. Sciacca thanks MITI CNRS (project COMPACT) and French Nantional research Agency (ANR-21-CE09-0017-01) for funding. This work received support from the French government under the France 2030 investment plan, as part of the Initiative d'Excellence d'Aix-Marseille Université - A*MIDEX.

References

1. Koenderink, A. F.; Alù, A.; Polman, A. Nanophotonics: Shrinking light-based technology. Science **2015**, 348, 516–521.

2. Choi, J. H.; Wang, H.; Oh, S. J.; Paik, T.; Jo, P. S.; Sung, J.; Ye, X.; Zhao, T.; Diroll, B. T.; Murray, C. B.; Kagan, C. R. Exploiting the colloidal nanocrystal library to construct electronic devices. Science **2016**, 352, 205–208.

3. Biswas, A.; Bayer, I. S.; Biris, A. S.; Wang, T.; Dervishi, E.; Faupel, F. Advances in top-down and bottom-up surface nanofabrication: Techniques, applications & future prospects. Advances in Colloid and Interface Science **2012**, 170, 2–27.

4. Marrian, C. R. K.; Tennant, D. M. Nanofabrication. Journal of Vacuum Science & Technology A: Vacuum, Surfaces, and Films **2003**, 21, 207–215.

5. Sciacca, B.; Van De Groep, J.; Polman, A.; Garnett, E. C. Solution-Grown Silver Nanowire Ordered Arrays as Transparent Electrodes. Advanced Materials **2016**, 28, 905–909.

6. Zhang, X.; Liu, H.; Tian, J.; Song, Y.; Wang, L. Band-Selective Optical Polarizer Based on Gold-Nanowire Plasmonic Diffraction Gratings. Nano Letters **2008**, 8, 2653–2658.

7. Cai, J.; Qi, L. Recent advances in antireflective surfaces based on nanostructure arrays. Mater. Horiz. **2015**, 2, 37–53.

8. Kraus, T.; Malaquin, L.; Schmid, H.; Riess, W.; Spencer, N. D.; Wolf, H. Nanoparticle printing with single-particle resolution. Nature Nanotechnology **2007**, 2, 570–576.

9. Flauraud, V.; Mastrangeli, M.; Bernasconi, G. D.; Butet, J.; Alexander, D. T. L.; Shahrabi, E.; Martin, O. J. F.; Brugger, J. Nanoscale topographical control of capillary assembly of nanoparticles. Nature Nanotechnology **2017**, 12, 73–80.

10. Kang, J.; Park, C.-G.; Lee, S.-H.; Cho, C.; Choi, D.-G.; Lee, J.-Y. Fabrication of high aspect ratio nanogrid transparent electrodes via capillary assembly of Ag nanoparticles. Nanoscale **2016**, 8, 11217–11223.

11. Sciacca, B.; Berkhout, A.; Brenny, B.; Oener, S.; van Huis, M.; Polman, A.; Garnett, E. Monocrystalline Nanopatterns Made by Nanocube Assembly and Epitaxy. Advanced Materials **2017**, 29, 1701064.

12. Capitaine, A.; Sciacca, B. Nanocube Epitaxy for the Realization of Printable Monocrystalline Nanophotonic Surfaces. Advanced Materials **2022**, 34, 2200364.

13. Hong, S.; Yeo, J.; Kim, G.; Kim, D.; Lee, H.; Kwon, J.; Lee, H.; Lee, P.; Ko, S. H. Nonvacuum, Maskless Fabrication of a Flexible Metal Grid Transparent Conductor by Low-Temperature Selective Laser Sintering of Nanoparticle Ink. ACS Nano **2013**, 7, 5024–5031, PMID: 23731244.

14. Brittman, S.; Oener, S. Z.; Guo, K.; Āboliņš, H.; Koenderink, A. F.; Garnett, E. C. Controlling crystallization to imprint nanophotonic structures into halide perovskites using soft lithography. J. Mater. Chem. C **2017**, 5, 8301–8307.

15. Massiot, I.; Cattoni, A.; Collin, S. Progress and prospects for ultrathin solar cells. Nature Energy **2020**, 5, 959–972.

16. Agrawal, H.; Garnett, E. Nanocube Imprint Lithography. ACS Nano **2020**, 14, 11009–11016.

17. Polman, A.; Atwater, H. A. Photonic design principles for ultrahigh-efficiency photovoltaics. Nature Materials **2012**, 11, 174–177.

18. Zhang, H.; Kinnear, C.; Mulvaney, P. Fabrication of Single-Nanocrystal Arrays. Advanced Materials **2020**, 32, 1–19.

19. Li, W.; Zhou, Y.; Howell, I. R.; Gai, Y.; Naik, A. R.; Li, S.; Carter, K. R.; Watkins, J. J. Direct Imprinting of Scalable, High-Performance Woodpile Electrodes for Three-Dimensional Lithium-Ion Nanobatteries. ACS Applied Materials and Interfaces **2018**, 10, 5447–5454.

20. Lee, H. J.; Oh, S.; Cho, K. Y.; Jeong, W. L.; Lee, D. S.; Park, S. J. Spontaneous and Selective Nanowelding of Silver Nanowires by Electrochemical Ostwald Ripening and High Electrostatic Potential at the Junctions for High-Performance Stretchable Transparent Electrodes. ACS Applied Materials and Interfaces **2018**, 10, 14124–14131.

21. Keunen, R.; MacOretta, D.; Cathcart, N.; Kitaev, V. Stable ligand-free stellated polyhedral gold nanoparticles for sensitive plasmonic detection. Nanoscale **2016**, 8, 2575–2583.

22. Eustis, S.; El-Sayed, M. A. Why gold nanoparticles are more precious than pretty gold: Noble metal surface plasmon resonance and its enhancement of the radiative and nonradiative properties of nanocrystals of different shapes. Chemical Society Reviews **2006**, 35, 209–217.

23. Baffou, G.; Quidant, R. Nanoplasmonics for chemistry. Chemical Society Reviews **2014**, 43, 3898–3907.

24. Dundar Arisoy, F.; Kolewe, K. W.; Homyak, B.; Kurtz, I. S.; Schiffman, J. D.; Watkins, J. J. Bioinspired Photocatalytic Shark-Skin Surfaces with Antibacterial and Antifouling Activity via Nanoimprint Lithography. ACS Applied Materials and Interfaces **2018**, 10, 20055–20063.

25. Yoon, G.; Kim, K.; Huh, D.; Lee, H.; Rho, J. Single-step manufacturing of hierarchical dielectric metalens in the visible. Nature Communications **2020**, 11.

26. Beaulieu, M. R.; Hendricks, N. R.; Watkins, J. J. Large-Area Printing of Optical Gratings and 3D Photonic Crystals Using Solution-Processable Nanoparticle/Polymer Composites. ACS Photonics **2014**, 1, 799–805.

27. Jo, H. B.; Byeon, K. J.; Lee, H.; Kwon, M. H.; Choi, K. W. Fabrication of ZnO nanostructures using UV nanoimprint lithography of a ZnO nano-particle dispersion resin. Journal of Materials Chemistry **2012**, 22, 20742–20746.

28. Oh, Y. S.; Choi, D. Y.; Sung, H. J. Direct imprinting of thermally reduced silver nanoparticles via deformation-driven ink injection for high-performance, flexible metal grid embedded transparent conductors. RSC Adv. **2015**, 5, 64661–64668.

29. Jiang, W.; Liu, H.; Yin, L.; Ding, Y. Fabrication of well-arrayed plasmonic mesoporous TiO_2/Ag films for dye-sensitized solar cells by multiple-step nanoimprint lithography. Journal of Materials Chemistry A **2013**, 1, 6433–6440.

30. Visser, D.; Chen, D. Y.; Désières, Y.; Ravishankar, A. P.; Anand, S. Embossed Mie resonator arrays composed of compacted TiO_2 nanoparticles for broadband anti-reflection in solar cells. Scientific Reports **2020**, 10.

31. Ko, S. H.; Park, I.; Pan, H.; Grigoropoulos, C. P.; Pisano, A. P.; Luscombe, C. K.; Fréchet, J. M. Direct nanoimprinting of metal nanoparticles for nanoscale electronics fabrication. Nano Letters **2007**, 7, 1869–1877.

32. Park, I.; Ko, S. H.; Pan, H.; Grigoropoulos, C. P.; Pisano, A. P.; Fréchet, J. M.; Lee, E. S.; Jeong, J. H. Nanoscale patterning and electronics on flexible substrate by direct nanoimprinting of metallic nanoparticles. Advanced Materials **2008**, 20, 489–496.

33. Modaresialam, M.; Chehadi, Z.; Bottein, T.; Abbarchi, M.; Grosso, D. Nanoimprint Lithography Processing of Inorganic-Based Materials. Chemistry of Materials **2021**, 33, 5464–5482.

34. Radha, B.; Lim, S. H.; Saifullah, M. S.; Kulkarni, G. U. Metal hierarchical patterning by direct nanoimprint lithography. Scientific Reports **2013**, 3.

35. Bin-Alam, M. S.; Reshef, O.; Mamchur, Y.; Alam, M. Z.; Carlow, G.; Upham, J.; Sullivan, B. T.; Ménard, J. M.; Huttunen, M. J.; Boyd, R. W.; Dolgaleva, K. Ultra-high-Q resonances in plasmonic metasurfaces. Nature Communications **2021**, 12, 974.

36. Wu, R.; Yang, B.; Zhang, C.; Huang, Y.; Cui, Y.; Liu, P.; Zhou, C.; Hao, Y.; Gao, Y.; Yang, J. Prominent Efficiency Enhancement in Perovskite Solar Cells Employing Silica-Coated Gold Nanorods. Journal of Physical Chemistry C **2016**, 120, 6996–7004.

37. Capitaine, A.; Sciacca, B. Monocrystalline Methylammonium Lead Halide Perovskite Materials for Photovoltaics. Advanced Materials **2021**, 33, 2102588.

38. Nagpal, P.; Lindquist, N. C.; Oh, S.-H.; Norris, D. J. Ultrasmooth Patterned Metals for Plasmonics and Metamaterials. Science **2009**, 325, 594–597.

39. Xia, Y.; Xiong, Y.; Lim, B.; Skrabalak, S. E. Shape-controlled synthesis of metal nanocrystals: Simple chemistry meets complex physics? Angewandte Chemie - International Edition **2009**, 48, 60–103.

40. Kothari, R.; Beaulieu, M. R.; Hendricks, N. R.; Li, S.; Watkins, J. J. Direct Patterning of Robust One-Dimensional, Two-Dimensional, and Three-Dimensional Crystalline Metal Oxide Nanostructures Using Imprint Lithography and Nanoparticle Dispersion Inks. Chemistry of Materials **2017**, 29, 3908–3918.

41. Yang, H. J.; He, S. Y.; Chen, H. L.; Tuan, H. Y. Monodisperse copper nanocubes: Synthesis, self-assembly, and large-area dense-packed films. Chemistry of Materials **2014**, 26, 1785–1793.

42. Clark, B. D.; Jacobson, C. R.; Lou, M.; Renard, D.; Wu, G.; Bursi, L.; Ali, A. S.; Swearer, D. F.; Tsai, A. L.; Nordlander, P.; Halas, N. J. Aluminum Nanocubes Have Sharp Corners. ACS Nano **2019**, 13, 9682–9691.

43. Wang, Y.; Zheng, Y.; Huang, C. Z.; Xia, Y. Synthesis of Ag nanocubes 18-32 nm in edge length: The effects of polyol on reduction kinetics, size control, and reproducibility. Journal of the American Chemical Society **2013**, 135, 1941–1951.

44. Kuo, C. H.; Chen, C. H.; Huang, M. H. Seed-mediated synthesis of monodispersed Cu_2O nanocubes with five different size ranges from 40 to 420 nm. Advanced Functional Materials **2007**, 17, 3773–3780.

45. Chen, H. S.; Wu, S. C.; Huang, M. H. Direct synthesis of size-tunable PbS nanocubes and octahedra and the pH effect on crystal shape control. Dalton Transactions **2014**, 44, 15088–15094.

46. Imran, M.; Ijaz, P.; Baranov, D.; Goldoni, L.; Petralanda, U.; Akkerman, Q.; Abdelhady, A.; Prato, M.; Bianchini, P.; Infante, I.; Manna, L. Shape-Pure, Nearly Monodispersed $CsPbBr_3$ Nanocubes Prepared Using Secondary Aliphatic Amines. Nano Letters **2018**, 18, 7822–7831.

47. Dang, F.; Mimura, K. I.; Kato, K.; Imai, H.; Wada, S.; Haneda, H.; Kuwabara, M. Growth of monodispersed SrTiO3 nanocubes by thermohydrolysis method. CrystEngComm **2011**, 13, 3878–3883.

48. Joshi, U. A.; Jang, J. S.; Borse, P. H.; Lee, J. S. Microwave synthesis of single-crystalline perovskite $BiFeO_3$ nanocubes for photoelectrode and photocatalytic applications. Applied Physics Letters **2008**, 92, 2006–2009.

49. Yang, S.; Gao, L. Controlled Synthesis and Self-Assembly of CeO_2 Nanocubes. Journal of the American Chemical Society **2006**, 128, 9330–9331.

50. Van De Groep, J.; Spinelli, P.; Polman, A. Transparent conducting silver nanowire networks. Nano Letters **2012**, 12, 3138–3144.

51. Moreau, A.; Ciracì, C.; Mock, J. J.; Hill, R. T.; Wang, Q.; Wiley, B. J.; Chilkoti, A.; Smith, D. R. Controlled-reflectance surfaces with film-coupled colloidal nanoantennas. Nature **2012**, 492, 86–89.

52. Mock, J. J.; Hill, R. T.; Degiron, A.; Zauscher, S.; Chilkoti, A.; Smith, D. R. Distance-Dependent Plasmon Resonant Coupling between a Gold Nanoparticle and Gold Film. Nano Letters **2008**, 8, 2245–2252, PMID: 18590340.

53. Hill, R. T.; Mock, J. J.; Hucknall, A.; Wolter, S. D.; Jokerst, N. M.; Smith, D. R.; Chilkoti, A. Plasmon Ruler with Angstrom Length Resolution. ACS Nano **2012**, 6, 9237–9246, PMID: 22966857.

54. Chikkaraddy, R.; Zheng, X.; Benz, F.; Brooks, L. J.; De Nijs, B.; Carnegie, C.; Kleemann, M. E.; Mertens, J.; Bowman, R. W.; Vandenbosch, G. A.; Moshchalkov, V. V.; Baumberg, J. J. How Ultranarrow Gap Symmetries Control Plasmonic Nanocavity Modes: From Cubes to Spheres in the Nanoparticle-on-Mirror. ACS Photonics **2017**, 4, 469–475.

55. Ansar, S. M.; Ameer, F. S.; Hu, W.; Zou, S.; Pittman, C. U.; Zhang, D. Removal of Molecular Adsorbates on Gold Nanoparticles Using Sodium Borohydride in Water. Nano Letters **2013**, 13, 1226–1229.

56. Xia, X.; Zeng, J.; Oetjen, L. K.; Li, Q.; Xia, Y. Quantitative Analysis of the Role Played by Poly(vinylpyrrolidone) in Seed-Mediated Growth of Ag Nanocrystals. Journal of the American Chemical Society **2012**, 134, 1793–1801, PMID: 22206387.

57. Oksenberg, E.; Shlesinger, I.; Xomalis, A.; Baldi, A.; Baumberg, J. J.; Koenderink, A. F.; Garnett, E. C. Energy-resolved plasmonic chemistry in individual nanoreactors. Nature Nanotechnology **2021**, 16, 1378–1385.

58. Parsegian, V. A. A Handbook for Biologists, Chemists, Engineers, and Physicists; Cambridge University Press, New York (USA), 2006.

59. Yu, K.; Hodges, C.; Biggs, S.; Cayre, O. J.; Harbottle, D. Polymer Molecular Weight Dependence on Lubricating Particle-Particle Interactions. Industrial and Engineering Chemistry Research **2018**, 57, 2131–2138.

60. Klein, J. Shear, friction, and lubrication forces between polymer-bearing surfaces. Annual Review of Materials Science **1996**, 26, 581–612.

61. Israelachvili, J. N. In Intermolecular and Surface Forces (Third Edition), third edition ed.; Israelachvili, J. N., Ed.; Academic Press, Waltham (USA), 2011; pp 253–289.

62. Koczkur, K. M.; Mourdikoudis, S.; Polavarapu, L.; Skrabalak, S. E. Polyvinylpyrrolidone (PVP) in nanoparticle synthesis. Dalton Trans. **2015**, 44, 17883–17905.

63. Zhang, Q.; Li, W.; Moran, C.; Zeng, J.; Chen, J.; Wen, L. P.; Xia, Y. Seed-mediated synthesis of ag nanocubes with controllable edge lengths in the range of 30-200 nm and comparison of their optical properties. Journal of the American Chemical Society **2010**, 132, 11372–11378.

64. Park, J. E.; Lee, Y.; Nam, J. M. Precisely Shaped, Uniformly Formed Gold Nanocubes with Ultrahigh Reproducibility in Single-Particle Scattering and Surface-Enhanced Raman Scattering. Nano Letters **2018**, 18, 6475–6482.

65. Fan, Q.; Yang, H.; Ge, J.; Zhang, S.; Liu, Z.; Lei, B.; Cheng, T.; Li, Y.; Yin, Y.; Gao, C. Customizable Ligand Exchange for Tailored Surface Property of Noble Metal Nanocrystals. Research **2020**, 2020, 2131806.

66. Roy, P.; Badie, C.; Claude, J.-B.; barulin, A.; Moreau, A.; Lumeau, J.; Abbarchi, M.; Santinacci, L.; Wenger, J. Preventing Corrosion of Aluminum Metal with Nanometer-Thick Films of Al_2O_3 Capped with TiO_2 for Ultraviolet Plasmonics. ACS Applied Nano Materials **2021**, 4, 7199.

67. Waxenegger, J.; Trügler, A.; Hohenester, U. Plasmonics simulations with the MNPBEM toolbox: Consideration of substrates and layer structures. Computer Physics Communications **2015**, 193, 138–150.

68. Hohenester, U. Simulating electron energy loss spectroscopy with the MNPBEM toolbox. Computer Physics Communications **2014**, 185, 1177–1187.

69. Hohenester, U.; Trügler, A. MNPBEM – A Matlab toolbox for the simulation of plasmonic nanoparticles. Computer Physics Communications **2012**, 183, 370–381.

70. Leith, D. Drag on Nonspherical Objects. Aerosol Science and Technology **1987**, 6, 153–161.